Mapping degenerate vortex states in a kagome lattice of elongated antidots via scanning Hall probe microscopy

C. Xue,[1,2,*] J.-Y. Ge,[2,†] A. He,[3] V. S. Zharinov,[2] V. V. Moshchalkov,[2] Y. H. Zhou,[4,5]
A. V. Silhanek,[6] and J. Van de Vondel[2,‡]

[1]*School of Mechanics, Civil Engineering and Architecture, Northwestern Polytechnical University, Xi'an 710072, China*
[2]*INPAC-Institute for Nanoscale Physics and Chemistry, KU Leuven, Celestijnenlaan 200D, B-3001 Leuven, Belgium*
[3]*College of Science, Chang'an University, Xi'an 710064, China*
[4]*Department of Mechanics and Engineering Sciences, Key Laboratory of Mechanics on Disaster and Environment in Western China attached to the Ministry of Education of China, Lanzhou University, Lanzhou 730000, China*
[5]*School of Aeronautics, Northwestern Polytechnical University, Xi'an 710072, People's Republic of China*
[6]*Experimental Physics of Nanostructured Materials, Q-MAT, CESAM, Université de Liège, B-4000 Sart Tilman, Belgium*

(Received 29 January 2017; revised manuscript received 1 May 2017; published 18 July 2017)

We investigate the degeneracy of the superconducting vortex matter ground state by directly visualizing the vortex configurations in a kagome lattice of elongated antidots via scanning Hall probe microscopy. The observed vortex patterns, at specific applied magnetic fields, are in good agreement with the configurations obtained using time-dependent Ginzburg-Landau simulations. Both results indicate that the long-range interaction in this nanostructured superconductor is unable to lift the degeneracy between different vortex states and the pattern formation is mainly ruled by the nearest-neighbor interaction. This simplification makes it possible to identify a set of simple rules characterizing the vortex configurations. We demonstrate that these rules can explain both the observed vortex distributions and the magnetic-field-dependent degree of degeneracy.

DOI: 10.1103/PhysRevB.96.024510

I. INTRODUCTION

The physics of quantized units of flux in a superconductor interacting with a pinning landscape continues to attract considerable academic interest due to the implications largely transcending the domain of superconductivity, such as Bose condensates [1,2], colloids [3,4], semiconductors [5,6], Mott insulator transition [7], vortex ice, spin ice, and charge ice [8–12], skyrmions [13,14], cold-atom trapping [15], etc. The appeal and advantage of superconducting systems is that the size and number of the particles can be tuned by changing the temperature and the magnetic field, respectively. In addition, the flexibility in the design and fabrication of artificial vortex traps in superconducting films has stimulated, during the past decade, an in-depth investigation of the interplay between pinning landscape and vortex pattern symmetry [16], influence of the pinning center's size and period [17–20], vortex rectification on a kagome-like array [21], competition between ordered and disordered defects [22–24], or pinning energy dispersion [25,26], to name a few.

It has been recognized that vortex traps arranged in complex units cells, such as honeycomb or kagome patterns [27,28], exhibit some properties unique to them. Indeed, (i) molecular dynamics simulations have revealed cooperative ring elementary excitations in a kagome periodic array of pinning sites when the temperature is varied slowly [29], (ii) commensurate pinning enhancement takes place at magnetic fields $H/H_1 = n/2$ (honeycomb) and $H/H_1 = n/3$ (kagome) rather than at the standard fields $H/H_1 = n$ [30], (iii) stronger enhancement of the depinning current is observed compared to a triangular lattice [30], (iv) spontaneous transverse voltage and jamming effect in a honeycomb array are generated by the dimerization of interstitial vortices [31], and (v) vortex interaction enhanced saturation number and caging effect can be observed [32]. Although substantial theoretical effort has been undertaken to understand the physics of these systems, the experimental investigations remain scarce. The few performed experiments relied on electrical transport measurements and, therefore, represent an indirect assessment of the actual dynamics of the vortex matter [27,32]. In recent years, a lot of effort has been devoted to develop techniques capable of visualizing the vortex distributions with single vortex resolution. These techniques allow one to validate the aforementioned theoretical predictions in a direct manner. Moreover, they open the possibility to determine the configurational entropy, which relies on counting the available states. This direct imaging of configurational entropy has successfully been performed in nanostructured magnetic systems [33,34]. Bearing in mind the tunability of a vortex system, this opens a new route to explore degeneracy and frustration in nanostructured superconductors.

In this paper we explore the vortex distribution using scanning Hall probe microscopy (SHPM) in a thin superconducting film with an artificially introduced kagome lattice consisting of elongated antidots [see Fig. 1(a)]. By performing consecutive field-cooling (FC) experiments we can visualize the resulting vortex distributions at different fractional matching fields. The main observation is that each FC experiment at a fixed magnetic-field value (between 0 and H_1) results in a different vortex configuration. These experiments indicate that a large set of vortex configurations exists with nearly the same energy. The resulting vortex patterns can be explained by the particular design of the elongated antidot structure and its impact on the different vortex-vortex interactions. First, the short-range interaction between vortices located in two neighbor antidots is enhanced due to the elongated shape of the antidots. This gives

*xuecun@nwpu.edu.cn
†junyi.ge@fys.kuleuven.be
‡joris.vandevondel@kuleuven.be

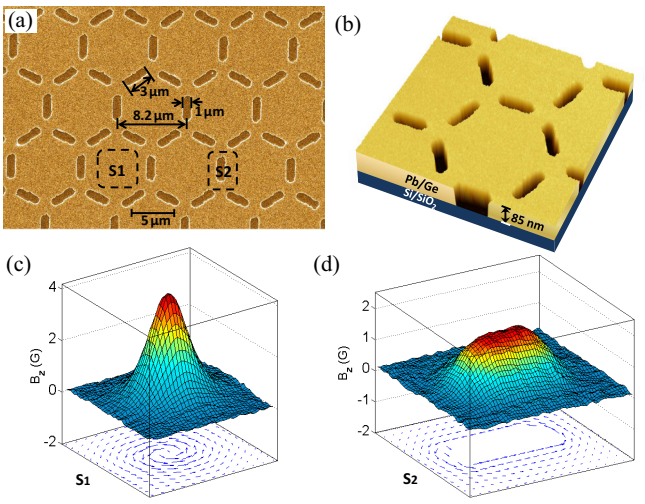

FIG. 1. (a) Scanning electron micrograph and (b) atomic force microscopy image of the investigated Pb film with an artificial kagome lattice of elongated antidots. Experimentally obtained out-of-plane component of the magnetic-field B_z and simulated current lines for (c) an interstitial vortex located in area S_1 and (d) a pinned vortex in area S_2. The locations of S_1 and S_2 are indicated in panel (a).

rise to very strong local constraints. In addition, the interaction between vortices separated by exactly one antidot (long-range interaction) is weaker and unable to differentiate between the various vortex distributions. As such, the long-range order is lifted, and the vortex patterns are determined by the specific local constraints. Moreover, the obtained degeneracy can easily be tuned by varying the applied magnetic field, which makes it an ideal toy model to explore degeneracy in physical systems.

II. SAMPLE AND EXPERIMENTS

Figures 1(a) and 1(b) show the kagome lattice of elongated antidots in an 85-nm-thick Pb film, fabricated using conventional electron-beam lithography, on a Si/SiO_2 substrate. The sample stage is cooled to 77 K using liquid nitrogen to ensure a homogeneous growth. A Ge layer with a thickness of 10 nm also is deposited on top of the Pb layer to protect it from oxidation. The source materials are 99.999%-pure Pb and 99.9999%-pure Ge. The external magnetic field is applied perpendicularly to the sample surface, and the vortex configurations are visualized directly using a-low temperature SHPM (with a magnetic-field resolution of 10^{-5} T and a temperature stability better than 1 mK) [35,36]. All the SHPM images of vortex patterns in our measurements are obtained by lifting the Hall cross about 500–800 nm above the sample surface at $T = 4.25$ K.

In analogy to other well-studied antidot systems [37,38], the elongated antidots act as pinning centers to trap vortices. Since, for a broad parameter range, the attractive vortex-pinning force is much stronger than the repulsive vortex-vortex interaction, the vortices prefer to occupy vacant antidots rather than forming an Abrikosov lattice. Figures 1(c) and 1(d) show the measured magnetic-field profiles and the simulated current lines for an interstitial and trapped vortex, respectively. These results clearly indicate that the pinned vortex is deformed strongly. As a result, the interaction between vortices will depend on their exact orientation. The short-range interaction between vortices located at neighbor antidots is very strong and will impose strict magnetic-field-dependent constraints on the vortex lattice. For example, the number of vortices observed in each unit cell perfectly corresponds to the applied field value at $H = H_1/3$, $2H_1/3$, and H_1.

At fields below H_1, the long-range interaction between vortices separated by an empty antidot also plays an important role in determining the energy of the vortex lattice. Previous SHPM experiments on nanostructured Pb superconductors in this field range show that the observed vortex patterns are the ones maximizing the intervortex distance [39,40]. In the present case, the anisotropy of the pinned vortices and the anisotropy of the superconducting film due to the elongated antidots in the introduced kagome lattice result in a complex vortex-vortex interaction. Its impact on the final vortex distribution, defined by the lowest-energy state, is difficult to predict. Therefore, time-dependent Ginzburg-Landau (TDGL) simulations are needed in order to gain insight and resolve the important factors determining the experimentally observed vortex patterns.

III. THEORETICAL FORMALISM

The simulations are derived based on the TDGL equations, which provide a very useful tool for modeling both dynamic and static superconducting properties. The normalized TDGL equations can be written as [41–43]

$$\partial_t \psi = (\nabla - i\mathbf{A})^2 \psi + \psi - |\psi|^2 \psi, \tag{1}$$

$$\sigma\, \partial_t \mathbf{A} = \mathbf{J}_s - \kappa^2 \nabla \times \nabla \times \mathbf{A}, \tag{2}$$

$$\mathbf{J}_s = \mathrm{Im}(\psi^* \nabla \psi) - \mathbf{A}|\Psi|^2, \tag{3}$$

where ψ, $\mathbf{A}$, and J_s are order parameter, vector potential, and supercurrent density, respectively. The length is made dimensionless in units of coherence length ξ, time in ξ^2/D where D is the diffusion coefficient, order parameter in $\psi_0 = \sqrt{|a|/b}$, and vector potential in $\sqrt{2}\kappa H_c \xi$ where $H_c = \sqrt{4\pi a^2/b}$.

The magnetic field can be derived by using the Biot-Savart law,

$$\mathbf{B}(\mathbf{r}) = \frac{\mu_0}{4\pi} \int_V \frac{\mathbf{J}_s(\mathbf{r}') \times (\mathbf{r} - \mathbf{r}')}{|\mathbf{r} - \mathbf{r}'|^3} d\mathbf{r}', \tag{4}$$

where $\mathbf{r} = (x, y, h)$, $\mathbf{r}' = (x', y', 0)$ and h is the distance between the Hall cross and the sample surface. The Gibbs free-energy density of the system in units of $H_c^2 V/8\pi$ can be calculated as [42]

$$G_t = G_h + G_p = V^{-1} \int_V [2(\mathbf{A} - \mathbf{A}_0)\mathbf{J}_s - |\psi|^4] d\mathbf{r}, \tag{5}$$

where $\mathbf{A}_0$ is the vector potential of the uniform magnetic field. We consider an infinite sample, and periodic boundary conditions are applied in the simulations. Because the thickness of the sample is sufficiently small, the variations of the order parameter and currents along the thickness can be neglected. To reproduce the stable vortex patterns observed in the field-cooling experiments, we start the simulations from different

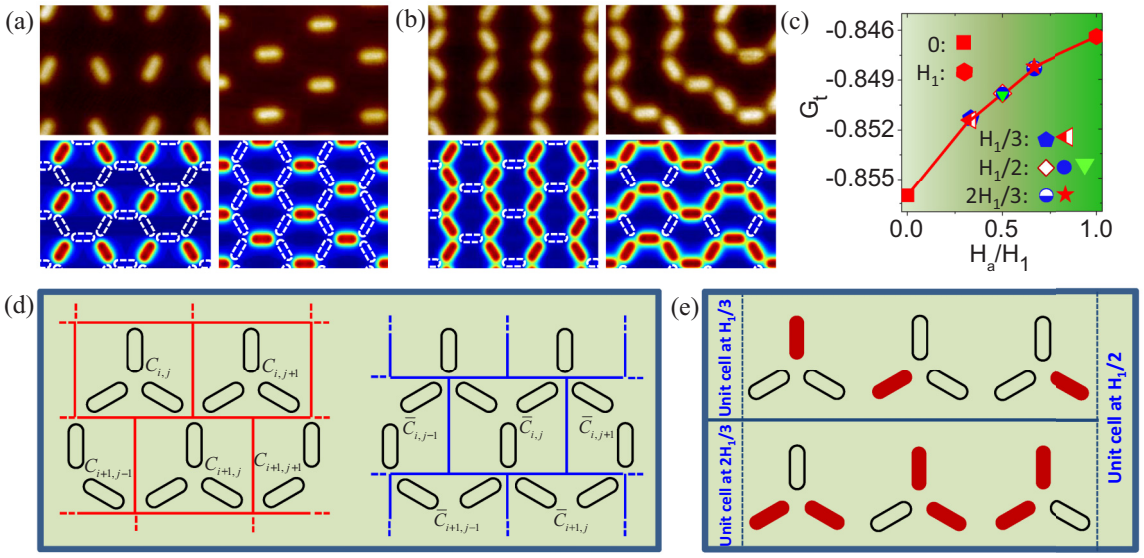

FIG. 2. (a) and (b) Two SHPM images (upper panels) and TDGL simulations (lower panels) of the vortex states in a kagome antibar lattice at $H_a = H_1/3$ and $2H_1/3$, respectively. (c) Free energy of the vortex state at $H_a = 0$ (red square), the two vortex lattice configurations shown in panel (a) at $H_1/3$ (red-white triangle and blue pentagon), the three vortex lattice configurations at $H_1/2$ shown in Fig. 4(b) (white diamond, blue circle, and green triangle), the two possible states shown in panel (b) at $2H_1/3$ (red pentagram and white-blue circle) and, finally, the vortex state shown in Fig. 5(b) at H_1 (red hexagon). (d) The unit cells (red) and conjugated unit cells (blue) in the kagome lattice. (e) Schematic of possible vortex arrangements in a unit cell at $H_a = H_1/3$, $2H_1/3$, and $H_1/2$.

randomly generated initial conditions [9]. Then we can obtain many vortex ground and metastable states. We find that the free energy of some vortex states is nearly the same, and these vortex configurations agree well with the experimental vortex patterns observed at specific applied magnetic fields.

IV. RESULTS AND DISCUSSIONS

In order to show the presence of degeneracy and obtain the constraints imposed by this particular nanopatterned system, we explore the vortex distributions at different fractional matching fields. Figures 2(a) and 2(b) show SHPM images and TDGL simulations of typical vortex states observed at $H_a = H_1/3$ and $2H_1/3$, respectively. Good agreement is observed between the simulated results (lower panels) and the experimentally obtained data (upper panels). Moreover, the square versus triangular packing of the vortices [shown in Fig. 2(a)] results in a distinct average vortex-vortex distance between both states. However, the observation of both vortex states indicates that the difference between the vortex interactions in the two states is too small to resolve. One could possibly argue that the elongated antidots in between vortices in the kagome lattice lower the free-energy difference between the square and the triangular vortex states. This can be clarified by removing the vacant elongated antidots in between vortices. Indeed, the TDGL simulations indicate that the elongated antidots in the kagome lattice effectively decrease the difference induced by the long-range interactions between the square and the triangular vortex patterns. At $2H_1/3$ the interpretation is analogous. The interactions between the nearest-neighbor vortices define strong local constraints, whereas very small energy differences (about ten thousandth in units of $H_c^2 V/8\pi$) exist between the vortex states arising from the interactions between vortices located at next-nearest-neighbor antidots. In addition, we have calculated the free energy as a function of the magnetic field, based on the TDGL simulations [see Fig. 2(c)]. The free energy for different vortex distributions, marked by different symbols, is indeed nearly the same. These results show that the long-range interaction is unable to resolve between different possible distributions. The free energy of vortex states at $H_1/2$ is situated at the midpoint between the vortex states at $H_1/3$ and $2H_1/3$ since the energy caused by vortex-vortex interactions increases linearly with an external applied field.

By analyzing the obtained experimental and simulated vortex patterns, we can identify common topological characteristics regarding the resulting vortex configurations. At $H_a = H_1/3$, exactly one-third of the antidots is filled with vortices. By assuring homogeneity of the equilibrium state, this constraint persists on a local scale, which results in the occupation of one antidot at each vertex of the system. This constraint is a natural consequence of a FC experiment since vortices are formed starting from a homogeneous field distribution. At $H_a = 2H_1/3$ exactly the complementary conditions are fulfilled: (i) Two-thirds of the elongated antidots are filled, and (ii) two antidots are occupied in each unit cell of the system. As seen in Fig. 2(b), these constraints result in the formation of parallel vortex strings at $2H_1/3$, which look like the domain walls in the superconductor.

The topological characteristics of the different degenerate vortex patterns can be deduced from simple filling rules imposed onto the occupation of the kagome lattice unit cell. This approach will allow us to calculate the degeneracy as a function of the applied magnetic field. As shown in Fig. 2(d), the kagome lattice can be divided into unit cells and conjugated unit cells, which are labeled as $C_{i,j}$ and $\overline{C}_{i,j}$,

respectively. The matrices $\mathbf{C} = [C_{i,j}]$ and $\overline{\mathbf{C}} = [\overline{C}_{i,j}]$ define the number of vortices in each unit cell and conjugated unit cell. The aforementioned constraints can now be written down explicitly for both magnetic-field values. In order to match the applied magnetic field, $\sum_{i,j}\{C_{i,j}\} = N/3$ at $H_1/3$ and $\sum_{i,j}\{C_{i,j}\} = 2N/3$ for $2H_1/3$ with N as the amount of unit cells in the sample. As a result of the second (local) constraint, $C_{i,j}$ has to be 1 at $H_1/3$, one-occupied/two-empty antidots, and 2 at $2H_1/3$, two-occupied/one-empty antidot, which are reminiscent of ice rules [8–10]. Figure 2(e) schematically presents three equivalent vortex arrangements in the cases of $C_{i,j} = 1$ and $C_{i,j} = 2$.

If the adjacent unit cells are noninteracting, the vortex distribution is highly degenerate, and the amount of degeneracy for both field values is 3^N. In the case of a long-range interaction the translational symmetry will be preserved, and only three possible distributions exist. As such, no real degeneracy (i.e., scaling with N) can be observed. However, in the case of a short-range interaction the constraints are weakened, and degeneracy is not fully lifted in this system. The nearest-neighbor interaction adds an additional constraint to the conjugated unit cells. More specifically, each conjugated unit cell must contain one vortex at $H_1/3$, i.e., $\overline{C}_{i,j} = 1$ and two vortices at $2H_1/3$, i.e., $\overline{C}_{i,j} = 2$. Although it reduces the amount of degeneracy, this constraint is much weaker than that imposed by the long-range interaction. Based on our numerical calculations the amount of degenerate vortex states is $Z < 1.644^N$ (see the Supplemental Material [44]).

Moreover, with the aforementioned rules we can also construct a possible vortex distribution on a larger scale. The middle panel of Fig. 3 shows a design of vortex distribution in the large area in which the red (blue) bars represent the vortex pattern at $H_a = H_1/3$ ($H_a = 2H_1/3$). Please note that the reverse

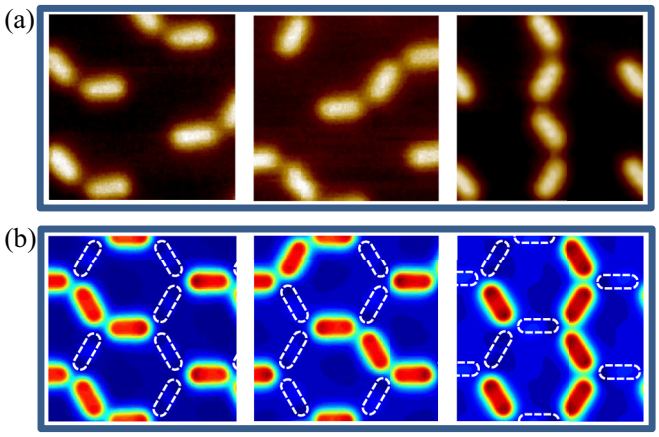

FIG. 4. (a) Experimental SHPM images of three different degenerate vortex states in a kagome lattice of elongated antidots at an applied field of $H_a = H_1/2$. (b) Three simulated vortex states at the same magnetic-field value.

vortex patterns at $H_1/3$ turn out to be vortex states at $2H_1/3$ and vice versa. By comparing this pattern with a variety of SHPM images at both magnetic-field values [upper and bottom panels of Fig. 2(e)] and keeping in mind the rotational symmetry of the system, we indeed can confirm that all obtained vortex distributions are reproduced by these simple rules.

As mentioned above, the number of particles can simply be tuned by merely increasing or decreasing the external magnetic field. Using this advantage, we also explore the vortex state degeneracy at $H_1/2$. As shown in Fig. 4(a), we observe completely different vortex states at $H_a = H_1/2$. To understand better the apparent randomness of the vortex distribution, we also perform numerical TDGL simulations

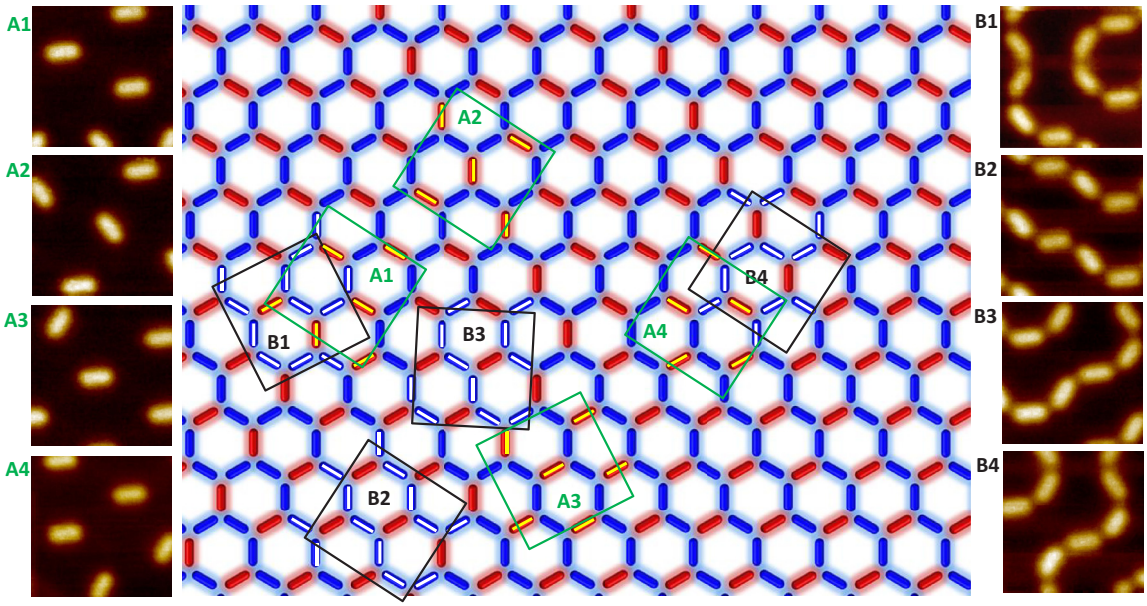

FIG. 3. Schematic of a possible degenerate vortex state based on the degeneracy rules of the system at $H_a = H_1/3$ and $2H_1/3$ (middle panel). The red bars represent the vortex configuration at $H_1/3$, and the blue bars represent the vortex state at $2H_1/3$. Experimental vortex states at $H_1/3$ (left panels A1–A4) and $2H_1/3$ (right panels B1–B4), which exactly correspond to the local vortex patterns (the red bars with the yellow lines in the four green boxes for the vortex configurations in the left panels and the blue bars with the white lines in the four black boxes for the vortex configurations in right panels) in the middle panel by rotating the boxes by 30°, 90°, 150°, 210°, 270°, or 330°.

for the vortex states at the corresponding field of $H_a = H_1/2$. Figure 4(b) shows the obtained results, which clearly resemble the vortex patterns observed by SHPM. Moreover, the TDGL simulations indicate that the free energy of these different vortex states is the same [see Fig. 2(c)].

Let us now identify the topological characteristics of the different degenerate vortex patterns in Figs. 4(a) and 4(b). First, since the applied magnetic field is $H_1/2$ and a FC procedure was used, only half of the antidots are occupied with vortices and the remaining half are empty. Second, the tendency of the system to keep a homogeneous field distribution results in the absence of completely empty unit cells and completely filled unit cells. As a result $C_{i,j}$ has to be 1, one-occupied/two-empty antidots, or 2, two-occupied/one-empty antidot, which are reminiscent of ice rules. The obtained patterns are a combination of the six building blocks [presented in Fig. 2(e)] used to construct the vortex distribution at $H_a = H_1/3$ and $H_a = 2H_1/3$. In this case, we easily can pinpoint the initial constraints $1 \leqslant C_{i,j} \leqslant 2$ and $\sum_{i,j}\{C_{i,j} - 1\} = N/2$. It is interesting to note that the reverse patterns of vortex states at $H_1/2$ also are degenerate vortex states. For instance, as shown in Fig. 4(b), the vacant antibars (white dashed bars) also are degenerate vortex states at $H_1/2$. If no interaction exists between these unit cells, the aforementioned constraints result in an amount of degeneracy equal to $Z = \frac{3^N N!}{[(N/2)!]^2}$. Based on Stirling's approximation, $Z \approx \sqrt{\frac{2}{\pi N}} 6^N$ (see the Supplemental Material [44]). However, also at this magnetic-field value two additional constraints appear due to the interplay between neighbor unit cells. These constraints can be well identified using the conjugated unit cells: (i) Similar to the regular unit cells, there must be one or two vortices in every conjugated unit cell, i.e., $1 \leqslant \overline{C}_{i,j} \leqslant 2$. (ii) The number of conjugated unit cells with one vortex must be $N/2$, i.e., $\sum_{i,j}\{\overline{C}_{i,j} - 1\} = N/2$.

Finally, a general constraint was observed, combining both the regular and conjugated unit cells in order to avoid the accumulation of one-vortex unit cells or two-vortex unit cells in a larger area (overall uniformity of the magnetic-field profile), and every unit cell and its three conjugated unit cells (also every conjugated unit cell and its three unit cells) are neither all two-vortex unit cells nor all one-vortex unit cells based on the experimental and simulated vortex patterns (see Fig. 4), i.e., $5 \leqslant C_{i,j} + \overline{C}_{i-1,j} + \overline{C}_{i,j-1} + \overline{C}_{i,j} \leqslant 7$, $5 \leqslant \overline{C}_{i,j} + C_{i,j} + C_{i,j+1} + C_{i+1,j} \leqslant 7$. Because of these constraints, the degeneracy is reduced. For example, the degeneracy in 16 unit cells is $Z < 6.17 \times 10^9$ (see the Supplemental Material [44]), which is much less than possible vortex states with 16 unit cells (5.54×10^{11}) in the noninteracting case. However, compared to $H_a = H_1/3$ or $2H_1/3$ the degeneracy is increased strongly at $H_a = H_1/2$.

It has already been well established that not all nanoscale ferromagnetic islands comply with ice rules in the spin ice system. In the vortex system, additional vortices (vortex defects) can be introduced by detuning the external field. Figure 5(a) shows the experimental SHPM vortex pattern at $H_a = 0.792$ G ($0.741 H_1$). The simulated result, shown in Fig. 5(c), is in very good agreement with the experimental result. Some of the vortex strings intersect at some vertices where three neighbor antibars are all occupied by vortices. Such defects will have an impact on the degeneracy of the total system. With increasing field, the amount of the defects increases, and the superconducting stripes are divided into more isolated areas. The increasing number of defects causes a reduction of degeneracy of the vortex states. Finally, as shown in Fig. 5(b), every antibar traps exactly one vortex to form a large vortex net at H_1. The vortex state at H_1 is unique, and degeneracy is completely suppressed.

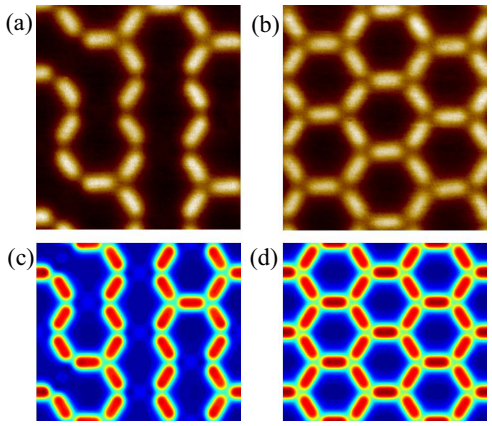

FIG. 5. (a) and (b) Experimental observation of vortex states in a kagome antibar lattice at $H_a = 0.792$ G (between $2H_1/3$ and H_1) and $H_a = H_1$ via SHPM. Simulated vortex distributions at $H_a = 0.801$ G and at $H_a = H_1$ are shown in panels (c) and (d), respectively.

V. CONCLUSION

To summarize, we investigate vortex matter in a superconducting film with a kagome lattice of elongated antidots. This particular structure enhances the first-neighbor vortex-vortex interaction, whereas the long-range vortex-vortex interaction is unable to lift the degeneracy between different possible distributions. As a result we observe many distinct vortex states and a large configuration entropy at several fractional matching fields. Based on the experimental data and TDGL simulations, we identified the rules characterizing the vortex configurations at $H_1/3$, $H_1/2$, and $2H_1/3$, respectively. In addition, vortex defects lead to a reduction of the degeneracy. The elongated antidot system in the form of a kagome antibar lattice provides new possibilities for studying vortex degeneracy using scanning Hall probe microscopy, and it demonstrates the potential of similar vortex systems as a highly tunable playground to explore the interplay between frustration and degeneracy.

ACKNOWLEDGMENTS

C.X. and A.H. acknowledge support by the Fundamental Research Funds for the Central Universities (Grants No. G2016KY0305, No. 3102017jc01003, and No. 310812171011). Y.H.Z., C.X., and A.H. acknowledge the National Natural Science Foundation of China (Grant No. 11421062) and the National Key Project of Magneto-Constrained Fusion Energy Development Program (Grant No. 2013GB110002). J.-Y.G, V.S.Z., J.V.d.V., and V.V.M. acknowledge support from the Methusalem funding by the Flemish government and the Flemish Science Foundation (FWO-Vl). The work of A.V.S. has been supported in part by PDR T.0106.16 of F.R.S.-FNRS.

[1] C. N. Weiler, T. W. Neely, D. R. Scherer, A. S. Bradley, M. J. Davis, and B. P. Anderson, Nature (London) **455**, 948 (2008).

[2] J. R. Abo-Shaeer, C. Raman, J. M. Vogels, and W. Ketterle, Science **292**, 476 (2001).

[3] P. T. Korda, G. C. Spalding, and D. G. Grier, Phys. Rev. B **66**, 024504 (2002).

[4] P. Tierno and T. M. Fischer, Phys. Rev. Lett. **112**, 048302 (2014).

[5] M. Berciu, T. G. Rappoport, and B. Jankó, Nature (London) **435**, 71 (2005).

[6] T. Richter, C. Blömers, H. Lüth, R. Calarco, M. Indlekofer, M. Marso, and T. Schäpers, Nano Lett. **8**, 2834 (2008).

[7] N. Poccia, T. I. Baturina, F. Coneri, C. G. Molenaar, X. R. Wang, G. Bianconi, A. Brinkman, H. Hilgenkamp, A. A. Golubov, and V. M. Vinokur, Science **349**, 1202 (2015).

[8] A. Libál, C. J. O. Reichhardt, and C. Reichhardt, Phys. Rev. Lett. **102**, 237004 (2009).

[9] M. L. Latimer, G. R. Berdiyorov, Z. L. Xiao, F. M. Peeters, and W. K. Kwok, Phys. Rev. Lett. **111**, 067001 (2013).

[10] P. A. McClarty, A. O'Brien, and F. Pollmann, Phys. Rev. B **89**, 195123 (2014).

[11] J. Trastoy, M. Malnou, C. Ulysse, R. Bernard, N. Bergeal, G. Faini, J. Lesueur, J. Briatico, and J. E. Villegas, Nat. Nanotechnol. **9**, 710 (2014).

[12] Y.-L. Wang, Z.-L. Xiao, A. Snezhko, J. Xu, L. E. Ocola, R. Divan, J. E. Pearson, G. W. Crabtree, and W.-K. Kwok, Science **352**, 962 (2016).

[13] S. Seki, X. Z. Yu, S. Ishiwata, and Y. Tokura, Science **336**, 198 (2012).

[14] J. Sampaio, V. Cros, S. Rohart, A. Thiaville, and A. Fert, Nat. Nanotechnol. **8**, 839 (2013).

[15] O. Romero-Isart, C. Navau, A. Sanchez, P. Zoller, and J. I. Cirac, Phys. Rev. Lett. **111**, 145304 (2013).

[16] R. B. G. Kramer, A. V. Silhanek, J. Van de Vondel, B. Raes, and V. V. Moshchalkov, Phys. Rev. Lett. **103**, 067007 (2009).

[17] A. V. Silhanek, W. Gillijns, M. V. Milošević, A. Volodin, V. V. Moshchalkov, and F. M. Peeters, Phys. Rev. B **76**, 100502(R) (2007).

[18] M. Motta, F. Colauto, W. A. Ortiz, J. Fritzsche, J. Cuppens, W. Gillijns, V. V. Moshchalkov, T. H. Johansen, A. Sanchez, and A. V. Silhanek, Appl. Phys. Lett. **102**, 212601 (2013).

[19] D. Ray, C. J. O. Reichhardt, B. Jankó, and C. Reichhardt, Phys. Rev. Lett. **110**, 267001 (2013).

[20] Y. L. Wang, M. L. Latimer, Z. L. Xiao, R. Divan, L. E. Ocola, G. W. Crabtree, and W. K. Kwok, Phys. Rev. B **87**, 220501(R) (2013).

[21] D. Perez de Lara, M. Velez, A. Gomez, F. Galvez, A. Alija, M. A. Garcia, J. I. Martin, E. M. Gonzalez, and J. L. Vicent, Supercond. Sci. Technol. **26**, 035016 (2013).

[22] C. J. Olson, C. Reichhardt, and S. Bhattacharya, Phys. Rev. B **64**, 024518 (2001).

[23] G. Pasquini, D. P. Daroca, C. Chiliotte, G. S. Lozano, and V. Bekeris, Phys. Rev. Lett. **100**, 247003 (2008).

[24] Y. L. Wang, L. R. Thoutam, Z. L. Xiao, B. Shen, J. E. Pearson, R. Divan, L. E. Ocola, G. W. Crabtree, and W. K. Kwok, Phys. Rev. B **93**, 045111 (2016).

[25] J. Gutierrez, A. V. Silhanek, J. Van de Vondel, W. Gillijns, and V. V. Moshchalkov, Phys. Rev. B **80**, 140514(R) (2009).

[26] G. Grimaldi, A. Leo, A. Nigro, A. V. Silhanek, N. Verellen, V. V. Moshchalkov, M. V. Milošević, A. Casaburi, R. Cristiano, and S. Pace, Appl. Phys. Lett. **100**, 202601 (2012).

[27] T. C. Wu, J. C. Wang, L. Horng, J. C. Wu, and T. J. Yang, J. Appl. Phys. **97**, 10B102 (2005).

[28] J. Cuppens, G. W. Ataklti, W. Gillijns, J. Van de Vondel, V. V. Moshchalkov, and A. V. Silhanek, J. Supercond. Novel Magn. **24**, 7 (2011).

[29] M. F. Laguna, C. A. Balseiro, D. Dominguez, and F. Nori, Phys. Rev. B **64**, 104505 (2001).

[30] C. Reichhardt and C. J. O. Reichhardt, Phys. Rev. B **76**, 064523 (2007).

[31] C. Reichhardt and C. J. O. Reichhardt, Phys. Rev. Lett. **100**, 167002 (2008).

[32] M. L. Latimer, G. R. Berdiyorov, Z. L. Xiao, W. K. Kwok, and F. M. Peeters, Phys. Rev. B **85**, 012505 (2012).

[33] R. F. Wang, C. Nisoli, R. S. Freitas, J. Li, W. McConville, B. J. Cooley, M. S. Lund, N. Samarth, C. Leighton, V. H. Crespi, and P. Schiffer, Nature (London) **439**, 303 (2006).

[34] P. E. Lammert, X. Ke, J. Li, C. Nisoli, D. M. Garand, V. H. Crespi, and P. Schiffer, Nat. Phys. **6**, 786 (2010).

[35] J. Y. Ge, J. Gutierrez, V. N. Gladilin, J. T. Devreese, and V. V. Moshchalkov, Nat. Commun. **6**, 6573 (2015).

[36] B. Raes, J. Van de Vondel, A. V. Silhanek, C. C. de Souza Silva, J. Gutierrez, R. B. G. Kramer, and V. V. Moshchalkov, Phys. Rev. B **86**, 064522 (2012).

[37] X. Hallet, M. Mátéfi-Tempfli, S. Michotte, L. Piraux, J. Vanacken, V. V. Moshchalkov, and S. Mátéfi-Tempfli, Small **5**, 2413 (2009).

[38] V. V. Moshchalkov, M. Baert, V. V. Metlushko, E. Rosseel, M. J. Van Bael, K. Temst, R. Jonckheere, and Y. Bruynseraede, Phys. Rev. B **54**, 7385 (1996).

[39] C. C. de Souza Silva, B. Raes, J. Brisbois, L. R. E. Cabral, A. V. Silhanek, J. Van de Vondel, and V. V. Moshchalkov, Phys. Rev. B **94**, 024516 (2016).

[40] J. Gutierrez, B. Raes, J. Van de Vondel, A. V. Silhanek, R. B. G. Kramer, G. W. Ataklti, and V. V. Moshchalkov, Phys. Rev. B **88**, 184504 (2013).

[41] W. D. Gropp, H. G. Kaper, G. K. Leaf, D. M. Levine, M. Palumbo, and V. M. Vinokur, J. Comput. Phys. **123**, 254 (1996).

[42] V. A. Schweigert and F. M. Peeters, Phys. Rev. B **57**, 13817 (1998).

[43] T. Winiecki and C. S. Adams, J. Comput. Phys. **179**, 127 (2002).

[44] See Supplemental Material at http://link.aps.org/supplemental/10.1103/PhysRevB.96.024510 for more detailed analysis on the amount of degeneracy at $H_1/3$, $2H_1/3$, and $H_1/2$.